Article

Alloy CsCd$_x$Pb$_{1−x}$Br$_3$ Perovskite Nanocrystals: The Role of Surface Passivation in Preserving Composition and Blue Emission

Muhammad Imran,* Julien Ramade, Francesco Di Stasio, Manuela De Franco, Joka Buha, Sandra Van Aert, Luca Goldoni, Simone Lauciello, Mirko Prato, Ivan Infante,* Sara Bals,* and Liberato Manna*

ACCESS | Metrics & More | Article Recommendations | Supporting Information

ABSTRACT: Various strategies have been proposed to engineer the band gap of metal halide perovskite nanocrystals (NCs) while preserving their structure and composition and thus ensuring spectral stability of the emission color. An aspect that has only been marginally investigated is how the type of surface passivation influences the structural/color stability of AMX$_3$ perovskite NCs composed of two different M^{2+} cations. Here, we report the synthesis of blue-emitting Cs-oleate capped CsCd$_x$Pb$_{1−x}$Br$_3$ NCs, which exhibit a cubic perovskite phase containing Cd-rich domains of Ruddlesden–Popper phases (RP phases). The RP domains spontaneously transform into pure orthorhombic perovskite ones upon NC aging, and the emission color of the NCs shifts from blue to green over days. On the other hand, postsynthesis ligand exchange with various Cs-carboxylate or ammonium bromide salts, right after NC synthesis, provides monocrystalline NCs with cubic phase, highlighting the metastability of RP domains. When NCs are treated with Cs-carboxylates (including Cs-oleate), most of the Cd^{2+} ions are expelled from NCs upon aging, and the NCs phase evolves from cubic to orthorhombic and their emission color changes from blue to green. Instead, when NCs are coated with ammonium bromides, the loss of Cd^{2+} ions is suppressed and the NCs tend to retain their blue emission (both in colloidal dispersions and in electroluminescent devices), as well as their cubic phase, over time. The improved compositional and structural stability in the latter cases is ascribed to the saturation of surface vacancies, which may act as channels for the expulsion of Cd^{2+} ions from NCs.
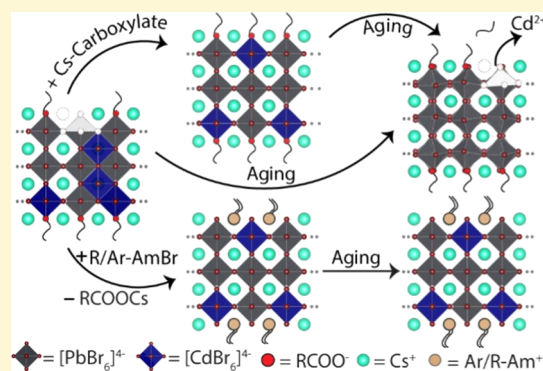
Halide perovskite nanocrystals (NCs) exhibit many exciting optical properties, such as near-unity photoluminescence quantum yield (PLQY), narrow emission linewidths, and band gap tunability.[1−6] The latter can be achieved by regulating the size of NCs and/or by adjusting their chemical composition.[7−34] Unfortunately, (and contrary to more traditional semiconductor NCs, such as CdSe) halide perovskite NCs have much lower colloidal stability, and small NCs, with sizes around 4−5 nm or below, are very unstable.[35,36] Considering the case of CsPbBr$_3$ as an example, 4−5 nm size NCs of this material have blue photoluminescence (PL) but their rapid coalescence and ripening, even when they are deposited in dry films, make their emission shift toward the green.[37−39] Tuning the emission color by adjustments in the chemical composition comes with its own shortcomings as well. Mixed halide anion compositions, for instance, APb(BrCl)$_3$ or APb(BrI)$_3$ (here A is typically Cs$^+$, methylammonium, or formamidinium) and also as bulk crystals, tend to undergo halide segregation under conditions such as an applied voltage bias or high irradiation flux, and their emission color changes with time.[40−48] Even perovskites with mixed A or B cation composition undergo cation

segregation.[49−51] Recent studies have shown that divalent cation (Mn^{2+}) substitution leads to the formation of Ruddlesden−Popper (RP) phases in Mn:doped CsPbCl$_3$ NCs.[52] Mixed cation strategies based on alloying univalent or divalent cations have been widely used in polycrystalline thin films to enhance the stability and power conversion efficiency of solar cells.[53] Also, in those cases, the resulting polycrystalline films are prone to ion segregation.[49,50] Various studies on thin films have revealed that ion migration (both cations and anions) is dominant at the grain boundaries and can be significantly reduced by efficient grain boundary passivation.[54−56] In comparison, the impact of surface coatings on the ion segregation, phase homogeneity, and color stability remains unclear for the NCs counterpart.

In the present work, we synthesize blue-emitting $CsCd_xPb_{1-x}Br_3$ NCs and show that the as-prepared NCs, which are coated with Cs-oleate ligands[57] (one of the standard ligand shells they have, as they are delivered from a typical synthesis) are spectrally unstable and evolve into green-emitting NCs upon aging. Atomically resolved high-angle annular dark-field scanning transmission electron microscopy (HAADF-STEM) reveals that the as-synthesized NCs are not structurally uniform: in addition to the perovskite phase, these NCs also contain Ruddlesden−Popper (RP) phases. This phase heterogeneity likely emerges at the synthesis step. We also demonstrate that Cd^{2+} ions, although distributed in the whole NCs, tend to accumulate in the RP domains by contracting the lattice parameters in those regions (Scheme 1,

Scheme 1. Structural/Compositional Evolution of Perovskite $CsCd_xPb_{1-x}Br_3$ NCs Coated with Cs-Carboxylate Ligands (a, b) or with Ammonium Bromide Ligands (c)[a]
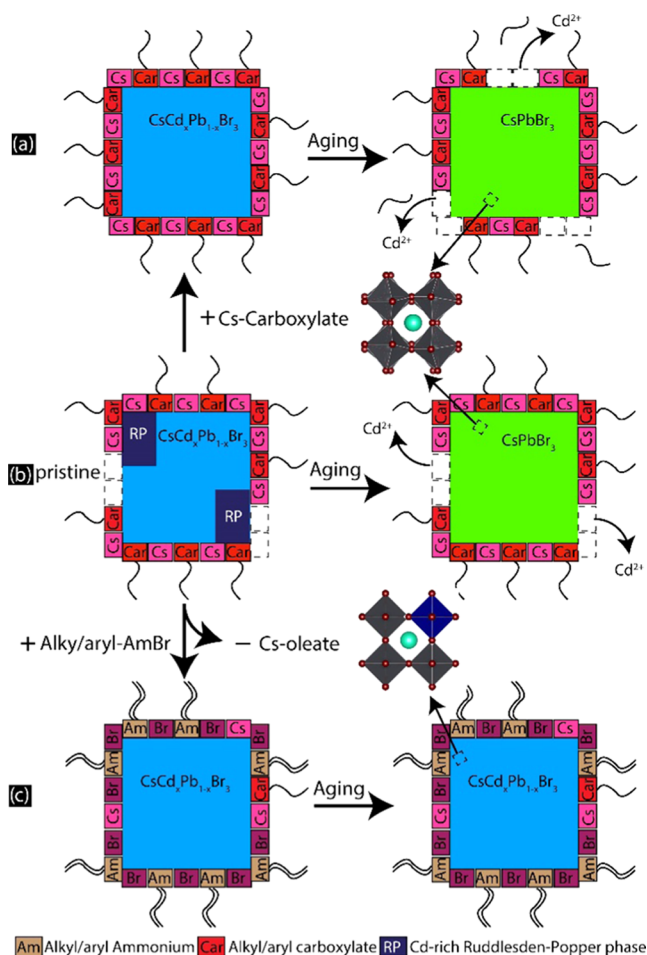
[a] The specific $CsCd_{0.25}Pb_{0.75}Br_3$ case is extensively studied in this work.

sketch b). Over aging, the RP regions undergo a transition to the perovskite phase and the NCs become monocrystalline. The same transition is accelerated when NCs are treated, postsynthesis, with Cs-carboxylates (such as Cs-oleate or Cs-phenylacetate) or with various alkyl/aryl ammonium salts (Scheme 1, sketches a and c). Apparently, these RP domains form a metastable state that, thanks to the softness of the NC lattice, can structurally reorganize easily.

Upon aging, two different fates are observed for the NCs depending on their surface ligands' composition: (1) Both the pristine sample (i.e., not treated postsynthesis with ligands) and the Cs-carboxylate-treated samples expel most of the Cd^{2+} ions (and evidently also a fraction of Br^- ions to maintain charge neutrality), likely due to an unstable surface ligand passivation of NCs under such circumstances. This loss of Cd^{2+} ions leads to a phase transformation of NCs from cubic perovskite to orthorhombic perovskite and to a shift in the emission color from blue to green (Scheme 1, sketches a and b). (2) When NCs are treated with primary or quaternary ammonium bromide ligands, they retain a uniform cubic $CsCd_xPb_{1-x}Br_3$ perovskite phase, from which Cd^{2+} ions are not expelled, so that they are able to preserve their blue emission over time both in colloidal dispersions and in electro-luminescent devices (Scheme 1, sketch c). A likely explanation for this structural (and emission color) stability is that ammonium bromide ligands are better able to saturate the surface AX vacancies, and this suppresses a potential channel for the expulsion of Cd^{2+} ions from NCs.

■ EXPERIMENTAL SECTION

Chemicals. Cadmium acetate dihydrate (($CdAc_2 \cdot 2H_2O$), 99.99%), lead acetate trihydrate (($PbAc_2 \cdot 3H_2O$), 99.99%), cesium carbonate (Cs_2CO_3, reagent Plus, 99%), benzoyl bromide (C_6H_5COBr, 97%), ethyl acetate (98.8%), toluene (anhydrous, 99.5%), phenethylammonium bromide (≥98%), didodecyldimethyl-lammonium bromide (DDABr), octadecene (ODE, technical grade, 90%), dimethyl sulfoxide-d_6 (DMSO, 99 atom % D) toluene-d8 (99 atom % D), and oleic acid (OA, 90%) were purchased from Sigma-Aldrich. Indium tin oxide (ITO)-patterned substrates, polystyrene sulfonate (PEDOT:PSS, AL 4083), poly(N,N9-bis(4-butylphenyl)-N,N9-bis(phenyl)-benzidine) (poly-TPD), and 2,2′,2″-(1,3,5-benzi-netriyl)-tris(1-phenyl-1-H-benzimidazole) (TPBi) were purchased from Ossila Ltd. Poly(9-vinylcarbazole) (PVK) and LiF were purchased from Sigma-Aldrich. Didodecylamine (97%) was purchased from TCI. Oleic acid was dried at 120 °C for an hour and stored in a nitrogen-filled glove box. All other chemicals were used without further purification.

Preparation of Oleylammonium Bromide. Oleylammonium bromide was prepared by reacting HBr with the corresponding oleyl amines in ethanol at 0 °C. Briefly, 50 mL of ethanol and 19 mmol of oleylamine were mixed in a 100 mL 2-neck flask and vigorously stirred. This mixture was cooled in an ice-water bath and 4.28 mL of HBr was added to it; the resulting mixture was allowed to react for 10 h under a N_2 flow. Then, the solution was dried under a vacuum and the solid product was purified by rinsing it with diethyl ether at least 3 times. The white precipitate was then dried overnight in a vacuum oven at 40° C and stored in the glove box for further use.

Synthesis of $CsCd_xPb_{1-x}Br_3$ NCs. Cs-oleate-capped NCs were prepared following our previously reported secondary-amine-based synthesis.[58] To synthesize $CsCd_xPb_{1-x}Br_3$ NCs with various Cd^{2+}/Pb^{2+} ratios, lead acetate trihydrate ($PbAc_2 \cdot 3H_2O$) was partially substituted with cadmium acetate dihydrate ($CdAc_2 \cdot 2H_2O$) in a direct synthesis (see Table 1 for the details on feed ratios of cadmium and lead precursors). Briefly, 0.15 mmol of divalent cation precursors ($CdAc_2 \cdot 2H_2O$ + $PbAc_2 \cdot 3H_2O$), 10 mg of cesium carbonate, and 10 mL of octadecene were mixed in a 25 mL 3-neck flask equipped with a thermocouple and a magnetic stirrer. The reaction mixture was degassed at room temperature for 5 min and under vacuum at 115 °C for 30 min and then filled with N_2. Then, the ligand mixture containing 1 mL of predried OA and 300 mg of didodecylamine dissolved in 1 mL of anhydrous toluene was rapidly injected. After the complete dissolution of the metal precursors, the temperature of the reaction mixture was decreased to 70 °C and 50 μL of a benzoyl bromide precursor diluted in 500 μL of anhydrous toluene was then injected into the mixture. After 45 s, the reaction mixture was cooled

Table 1. Reaction Conditions for the Synthesis of $CsCd_xPb_{1-x}Br_3$ NCs (Stoichiometries are estimated via Scanning Electron Microscopy-energy-dispersive spectrometry (SEM-EDS))

NC stoichiometry	metal precursors (M^{2+}) used in the synthesis (mmol)		PL peak position (nm)	PL line width (nm)
	$CdAc_2 \cdot 2H_2O$	$PbAc_2 \cdot 3H_2O$		
$CsPbBr_3$	0	0.15	507	16
$CsCd_{0.08}Pb_{0.92}Br_3$	0.05	0.10	496	18
$CsCd_{0.12}Pb_{0.88}Br_3$	0.075	0.075	484	20
$CsCd_{0.25}Pb_{0.75}Br_3$	0.1	0.05	476	24
$CsCdBr_3$ (main product)	0.125	0.025	nonemissive	

to room temperature in an ice-water bath. Thereafter, 12 mL of anhydrous ethyl acetate was added into the crude solution and centrifuged at 12 000 revolutions per minute (rpm) for 10 min. The precipitate was re-dispersed in 5 mL of toluene for further use.

Ligand Exchange. For the ligand-exchange reactions, the crude solution of NC was divided into 6 parts (2 mL each), one fraction was purified as it is and was used as a reference (pristine samples). Each of the remaining fractions was mixed with a toluene solution containing the ligands (Cs-oleate, Cs-phenylacetate, oleylammonium bromide, phenethylammonium bromide, didodecyldimethylammonium bromide) (2 mL, 50 mM) and the resulting mixture was vigorously stirred for 2 min. Thereafter, the NCs were washed with ethyl acetate (10 mL) or methyl acetate and re-dispersed in 5 mL of anhydrous toluene. The toluene dispersion of the NCs was centrifuged once again (at 6000 rpm for 10 min), the colloidally unstable fraction was discarded and the supernatant was collected for further use.

X-ray Powder Diffraction (XRPD) Characterization. The XRPD analysis was performed on a PANanalytical Empyrean X-ray diffractometer, equipped with a 1.8 kW Cu Kα ceramic X-ray tube, operating at 45 kV and 40 mA, and a PIXcel^{3D} 2 × 2 area detector. To avoid the preferred orientation effect, the concentrated dispersions of NCs were mixed with fumed silica powder prior to their deposition on a zero-diffraction silicon substrate. All of the diffraction patterns reported here were collected at room temperature under ambient conditions using the parallel beam geometry and symmetric reflection mode. Postacquisition XRPD data analysis was carried out using the HighScore 4.1 software from PANalytical.

Transmission Electron Microscopy (TEM) Characterization. Bright-field TEM images of the NC samples were acquired with a JEOL-1100 transmission electron microscope operating at an acceleration voltage of 100 kV. Samples were prepared by drop-casting diluted solutions of NCs onto the carbon film-coated 200 mesh copper grids for low-resolution TEM.

High-Resolution High Angle Annular Dark-Field Scanning Transmission Electron Microscopy Characterization. High-resolution HAADF-STEM images were acquired with a probe-corrected cubed FEI Titan microscope operating at 300 kV with a probe semiconvergence angle of 20.5 mrad. Qualitative analyses of column intensities and column-to-column distances were performed using StatSTEM.[59] The total scattered intensity and location of all atomic columns were determined by fitting Gaussian functions to these columns.

Scanning Electron Microscopy (SEM) Characterization. A JEOL JSM-7500FA microscope (Jeol, Tokyo, Japan) in a high-vacuum mode, with an acceleration voltage of 5 kV and backscattered electrons was used for the EDS analysis.

UV−Vis Absorption and PL Measurements. The UV−visible absorption spectra were recorded using a Varian Cary 300 UV−vis absorption spectrophotometer. The PL spectra were measured on a Varian Cary Eclipse spectrophotometer using an excitation wavelength (λ_{ex}) of 350 nm for all of the samples. Samples were prepared

by diluting NC solutions in toluene, in quartz cuvettes with a path length of 1 cm.

PL Quantum Yields and Time-Resolved PL Measurements. Photoluminescence quantum yields (PLQYs) of NC samples were measured using an Edinburgh FLS900 fluorescence spectrometer equipped with a xenon lamp, a monochromator for steady-state PL excitation, and a time-correlated single-photon counting unit coupled with a pulsed laser diode (λ_{ex} = 405 nm, pulse width = 50 ps) for time-resolved PL. The PLQY was measured using a calibrated integrating sphere (λ_{ex} = 350 nm for all $CsCd_xPb_{1-x}Br_3$ nanocube samples). All NC dispersions were diluted to an optical density of 0.1 at the corresponding excitation wavelength to minimize reabsorption of the emitted light.

NMR characterization. All of the NMR spectra were acquired on Bruker Avance 400 MHz spectrometer, supplied with a BBI probe. NCs and free ligands were dispersed in 600 μL of deuterated toluene, and transferred into 5mm disposable tubes (Bruker) for the ^{1}H NMR analyses that were performed at 300 K as follows: 64 scans were accumulated using 65 536 data points, an inter-pulses delay of 30 s, over a spectral width of 20.55 ppm, with the offset positioned at 6.18 ppm, and the receiver gain fixed (9). An exponential line broadening equivalent to 0.3 Hz was applied to FIDs before the Fourier transform. The spectra, manually phased and automatically baseline-corrected, were referred to the not-deuterated residual toluene peak, calibrated at 7.09 ppm. For ligands shell composition analysis, the NCs dissolved in 300 μL of deuterated DMSO were transferred into 3 mm disposable tubes (Bruker). The 90° pulse was optimized on each sample tube by an automatic pulse calculation routine,[60] and the q ^{1}H NMR was acquired with the previous acquisition parameters, except for the number of transients and the receiver gain that were increased to 128 and to 64, respectively. Processing parameters were identical to the previous experiment. The spectrum was referred to the not-deuterated residual DMSO peak, set at 2.50 ppm.

Two-Dimensional (2D) Nuclear Overhauser Effect Spectroscopy (^{1}H-^{1}H NOESY). The experiment (noesygpph, Bruker library)[61] was acquired with 32 scans, a relaxation delay of 2 s, a mixing time of 300 ms, 2048 digit points in the direct dimension, and 256 increments.

X-ray Photoelectron Spectroscopy (XPS) Characterization. Measurements were performed on a Kratos Axis Ultra DLD spectrometer, using a monochromatic Al Kα source (15 kV, 20 mA). The photoelectrons were detected at a take-off angle of ϕ = 0° with respect to the surface normal. The pressure in the analysis chamber was kept below 7 × 10^{-9} Torr for data acquisition. The data was converted into the VAMAS format and processed using CasaXPS software, version 2.3.22. The binding energy (BE) scale was internally referenced to the C1's peak (BE for C−C = 284.8 eV).

Device Fabrication and Characterization. Glass slides with patterned ITO were cleaned via immersion in acetone for 30 min, rinsed with isopropanol, and exposed to O$_2$ plasma. Device fabrication started with spin-coating of the PEDOT:PSS in air at 4000 rpm followed by annealing in air at 120 °C for 30 min. Afterward, the substrates were transferred into a N$_2$-filled glovebox where the hole-transport layer was prepared as follows: spin-coating of poly-TPD solution (2 mg/mL) in chlorobenzene at 2000 rpm for 40 s. The obtained poly-TPD film was then annealed at 110 °C for 20 min inside the glovebox, and the PVK film was prepared on top via spin-coating of a chlorobenzene solution (4 mg/mL) at 2000 rpm. The NC active layer was then prepared via spin-coating of a toluene solution on top of the PVK at 2000 rpm. The substrates were then transferred to a thermal evaporator inside the glovebox where TPbi/LiF/Al was deposited. The obtained LEDs were finally encapsulated using a coverslip and an epoxy resin. The current−voltage−luminance characteristics were measured using a Keithley 2636 source-measure unit coupled to a calibrated PDA 100 A Si switchable gain detector from Thorlabs. The system was controlled via a LabView interface. The output of the Si detector was converted into power (photon flux) using the responsivity of the detector. The external quantum efficiency (EQE) was calculated as the ratio of the photon flux and

the driving current of the device. The electroluminescence (EL) spectra were collected using an Ocean Optics HR4000 spectrometer.

Computational Modeling. Band structure calculations were performed at the density functional theory level using the Perdew–Burke–Ernzerhof (PBE) exchange–correlation functional,[62] as implemented in the VASP 6.1 package.[63,64] We employed a k mesh grid of $4 \times 4 \times 4$ for the Brillouin zone integration and a kinetic energy cutoff of 400 eV. The atomic positions and the lattice parameters were both relaxed until the forces were smaller than 0.001 Hartree/Angstrom. For the pure bulk $CsPbBr_3$ system, we employed a $1 \times 1 \times 1$ orthorhombic (*Pnma* symmetry) unit cell, whereas for the alloyed bulk $CsCd_{0.25}Pb_{0.75}Br_3$ we started from a cubic ($Pm\overline{3}m$ symmetry) $2 \times 2 \times 2$ unit cell, where 2 out of 8 Pb^{2+} ions were replaced with 2 Cd^{2+} ions. Spin–orbit effects were also included in the band structure calculations. The geometries and electronic structures of the alloyed $CsCd_{0.25}Pb_{0.75}Br_3$ nanoclusters were computed on charge-balanced NCs of about 3nm in size. These atomistic simulations were carried out also at the density functional theory (DFT)/PBE level of theory[62] but with the CP2K 6.1 package.[65] Here, we included a double-ζ basis set plus polarization functions on all atoms with effective-core potential for the inner electrons. Further details on the model systems employed are provided in the main text.

■ RESULTS AND DISCUSSION

In this work, we used a modified version of our previously reported synthesis that employs oleic acid and a secondary amine as surfactants.[58] To prepare $CsCd_xPb_{1-x}Br_3$ NCs, benzoyl bromide was injected into a solution containing cesium, cadmium, and lead oleates in the presence of didodecylamine. As discussed in our earlier work,[58] NCs prepared with this method are exclusively coated with Cs-oleate ligands, with didodecylamine acting only as a regulator of the overall growth kinetics. Henceforth, the NCs purified directly after the synthesis with ethyl acetate will be referred to as "pristine", and the reader should recall that they are coated with Cs-oleate. For the ligand-exchange reaction, the crude solution of NCs was mixed with a toluene solution of Cs-carboxylate or ammonium bromide salts. Thereafter, ethyl acetate was added to the crude solution, and the NCs were separated by centrifugation and redispersed in toluene (see the Experimental Section for details). We prepared several batches of $CsCd_xPb_{1-x}Br_3$ NCs by systematically varying the feed ratios of cadmium and lead ions in the synthesis while all of the other reaction conditions were kept constant. We observed the formation of regularly cubic-shaped NCs in all mixed-cation compositions, as revealed in the TEM images of Figure 1a–d. The XRPD analysis of the corresponding samples evidenced slight shifts in the peaks toward higher angles compared to the reference $CsPbBr_3$, suggesting a decrease in the cell volume due to the partial substitution of lead with cadmium. Furthermore, the XRPD patterns at a higher cadmium content closely match with the cubic phase (see Figure S1 of the Supporting Information (SI)). Based on the compositional analysis by SEM-energy dispersive X-ray spectroscopy (EDX), the Cd/Pb ratio in the NCs was correlated with the molar Cd/Pb feed ratio in the synthesis. We observed that the maximum extent of substitution of Pb^{2+} with Cd^{2+} ions was 25 ± 2% (obtained for a Cd/Pb feed ratio of 2:1), whereas working at higher Cd/Pb feed ratios led to the formation of non-luminescent $CsCdBr_3$ NCs as the main product (see Figure S2). Such compound has a hexagonal, non-perovskite phase, formed by chains of edge-sharing $[CdBr_6]^{4-}$ octahedra.

UV–vis optical absorption and photoluminescence (PL) spectra recorded on the colloidal dispersions of $CsCd_xPb_{1-x}Br_3$ NCs immediately after the synthesis evidenced a progressive
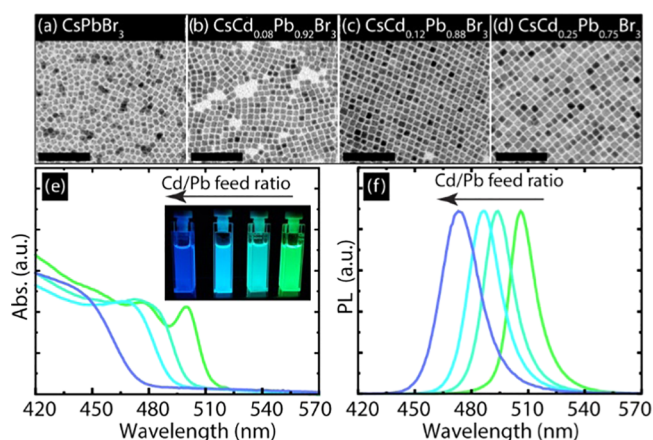

Figure 1. (a−d) TEM images evidencing size and shape uniformity of $CsCd_xPb_{1-x}Br_3$ NCs prepared by varying the feed ratios of cadmium and lead ions in the synthesis, while all of the other reaction conditions were kept constant; see the Experimental Section and Table 1 for details (scale bars are 100 nm). (e−f) Optical absorption and PL spectra recorded in toluene dispersions for all of the samples.

blue shift in their absorbance and PL spectra at the increasing substitution of Pb^{2+} with Cd^{2+} ions (i.e., x ranging from 0 to 0.25). In particular, the PL peak position shifted from 507 to 476 nm (see Figure 1e−f). However, we found that the emission color of the sample was not stable over time and turned green upon aging.

In an attempt to stabilize the emission color, especially for the bluest-emitting NCs ($CsCd_{0.25}Pb_{0.75}Br_3$), we tried various postsynthesis surface treatments. To this aim, the crude NC solution obtained from the synthesis was treated with various ligands, such as Cs-oleate, Cs-phenylacetate (Cs-PhAce), oleylammonium bromide (OLABr), phenethylammonium bromide (PhEABr), and didodecyl dimethylammonium bromide (DDABr) and then washed with ethyl acetate (or methyl acetate). The reader might be induced to think that the Cs-oleate-treated NCs and the pristine NCs should have exactly the same surface chemistry, as Cs-oleate is indeed the ligand shell present after the synthesis. However, it is likely for the Cs-oleate-treated NCs to have a higher fraction of surface sites passivated by ligands than the pristine NCs and indeed the two samples did not behave identically, as will be shown later.

Based on TEM, the ligand exchange did not alter the shape and size distribution of the NCs, except for the Cs-PhAce case (Figure S3a−f). The optical features of the freshly prepared and of the aged NC dispersions are compared in Figures 2a−c, S3g−l, and S4a−l. The freshly prepared ligand-exchanged NCs had essentially the same emission spectrum as the pristine NCs, with PL around 475−480 nm, except for the Cs-PhAce case (emission at 485 nm); see Figures 2a and S3g−l. However, upon aging, the emission spectrum of the pristine and Cs-carboxylate-treated samples (both Cs-oleate and Cs-PhAce) began to shift considerably toward the green, with the PL peak moving to ∼510 nm over 14 days of storage under air. Over the same time span, the emission from NCs coated with ammonium bromide ligands shifted much less (about 10 nm), and the one from the DDABr-coated sample remained practically unchanged (Figure 2a, see also Figure S4a−l). The trends in PLQY are reported in Figures 2b and S4m−r. The freshly prepared pristine NCs (PL peak at 478 nm) were weakly emissive, with a PLQY of 5 ± 0.5%, and the exchange with Cs-carboxylates did not improve their PLQY further. The
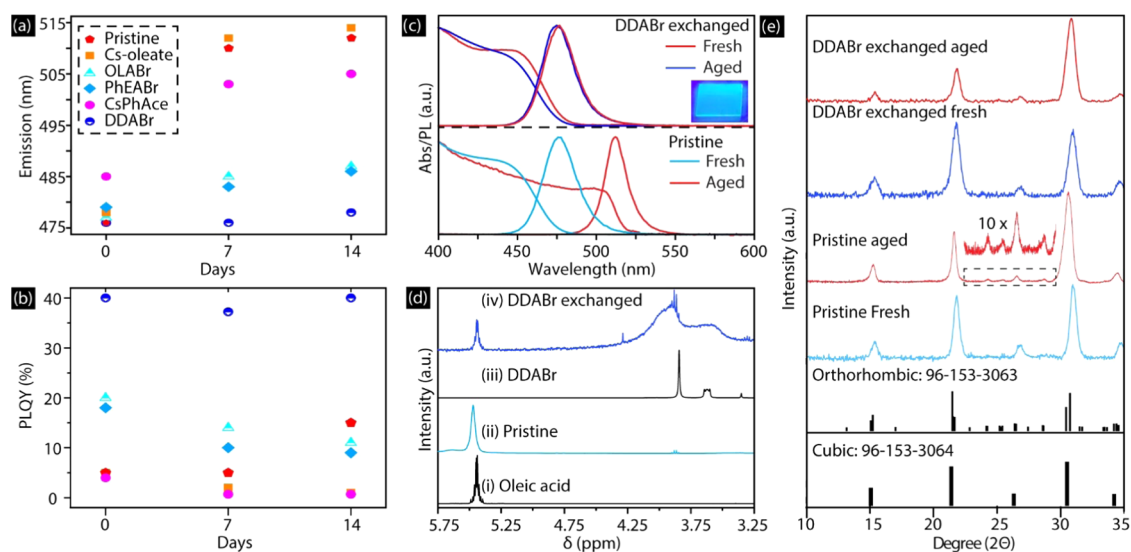
Figure 2. (a) Evolution of PL spectra recorded in colloidal dispersions upon aging for pristine and NCs treated with various ligands (optical absorption and PL spectra of the corresponding samples are reported in Figure S3), and the changes in PLQYs upon aging for the corresponding samples are reported in panel (b). (c) Optical absorption and PL spectra of two representative samples (pristine and DDABr-exchanged) recorded after the synthesis (fresh) and over storage in ambient air for 14 days. (d) Liquid-state ^1H NMR spectra of D-toluene solutions of oleic acid (i), pristine $CsCd_{0.25}Pb_{0.75}Br_3$ NCs (ii), DDABr (iii) and NCs after DDABr treatment. (e) XRPD patterns of pristine and DDABr-exchanged sample (fresh) and after two weeks of aging along with the bulk reference pattern for cubic and orthorhombic phases for $CsPbBr_3$.

increase in PLQY was much noticeable for the ammonium-bromide-exchanged samples, peaking at 40 ± 4% for the DDABr case. Here again, the DDABr-coated NCs were the best sample, retaining their initial emission efficiency over time, while all of the other samples experienced a decrease in the PLQY. A notable exception was the pristine NCs, for which an increase in the PLQY was measured over time, but this is also a sample that over time lost a considerable amount of Cd^{2+} ions (see later), hence approaching a quasi-pure $CsPbBr_3$ composition. A direct comparison of the optical behaviors of the two extreme samples (namely, the pristine NCs and the DDABr-exchanged ones) is given in Figure 2c (here, spectra are normalized), while their TEM images and PL lifetimes are reported in Figures S5−S6 and Table S1. The absorption and the emission features of the pristine sample changed considerably over time, while the DDABr sample was much less affected, with the PL peak position and linewidth remaining practically unchanged. As the DDABr ligand exchange appeared to be the best strategy to preserve the emission characteristics, we then extended this treatment to $CsCd_xPb_{1-x}Br_3$ NCs with other compositions (from $x = 0$ to 0.12). The PLQY of the freshly prepared DDABr-treated $CsCd_xPb_{1-x}Br_3$ NCs in colloidal dispersion decreased with an increase in cadmium incorporation from 85 ± 8% for $x = 0$ to 40 ± 4% for $x = 0.25$, and the average PL lifetime increased from 5.5 to 26.48 ns (see Figures S5−S8 and Tables S1−S2).

Next, we performed a detailed investigation of the surface and structural composition of the pristine and DDABr-exchanged samples, which correspond to the worst- and best-performing samples, respectively. Similar to a previous work of ours,[66] we performed liquid-state ^1H NMR spectroscopy to assess their surface chemistry. Figure 2d shows the ^1H NMR spectra of pristine (ii) and of the DDABr-exchanged NCs (iv) along with free ligands, oleic acid (i), and DDABr (iii) recorded in d-toluene. ^1H NMR analysis of the pristine sample indicated the presence of significantly broadened resonances around 5.47 ppm, as is expected for molecules

bound to an NC. This was further confirmed by the 2D ^1H NOESY (see Figure S9), which featured negative NOE signals (red, typical signature of ligands bound to the surface of NCs with longer correlation times) rather than the positive NOE signal (blue),[67−70] thus confirming that the as-synthesized and purified NCs were exclusively coated with oleate molecules. Similarly, for the DDABr-exchanged sample, the ^1H NMR resonances around 4.0 and 3.6 ppm broadened and shifted downfield compared to the corresponding free ligands, a proof that the ligand exchange was successful and that DDABr was bound to the surface of the NCs. The additional sharp and resolved signal at ca. 5.43 ppm arises from residual, free oleic acid molecules (see Figure S10). This was indeed supported by the 2D ^1H NOESY featuring negative (red) NOE signal for DDA (didodecyldimethyl ammonium) ligands and the positive (blue) NOE signal for oleic acid, thereby corroborating the interaction of the former (DDA) only with the surface of NCs (see Figure S11). To determine the content of organic species in the DDABr-exchanged sample, we dissolved NCs in deuterated dimethyl sulfoxide (DMSO) and performed quantitative NMR (q ^1H NMR) analysis (Figure S12). The ratio between the integrated peak intensities of vinyl protons of oleic acid and methyl moiety on the nitrogen of DDABr, each normalized for the number of resonances generating the signals, revealed that 86% of ligands are didodecyldimethyl ammonium and 14% are oleate species. This was further supported by XPS analysis showing no signature of nitrogen (which we consider as a marker for the presence of ammonium species on the surface of NCs) in the pristine sample, while the DDABr-exchanged NCs evidenced the presence of N (see Figure S13). Finally, the compositional analyses (by XPS, TEM-EDX, and SEM-EDX) of both pristine and the DDABr-exchanged samples are reported in Table S3 and Figure S14. According to both analyses, upon DDABr exchange, the Cs/(Cd + Pb) ratio decreased (from 1.24 to 1.05 (XPS) and from 1.13 to 1 (SEM-EDS)) and the Br/(Cd+Pb) ratio increased (from 2.68 to 2.89 (XPS) and from 2.83 to 3.21 (SEM-EDX)).
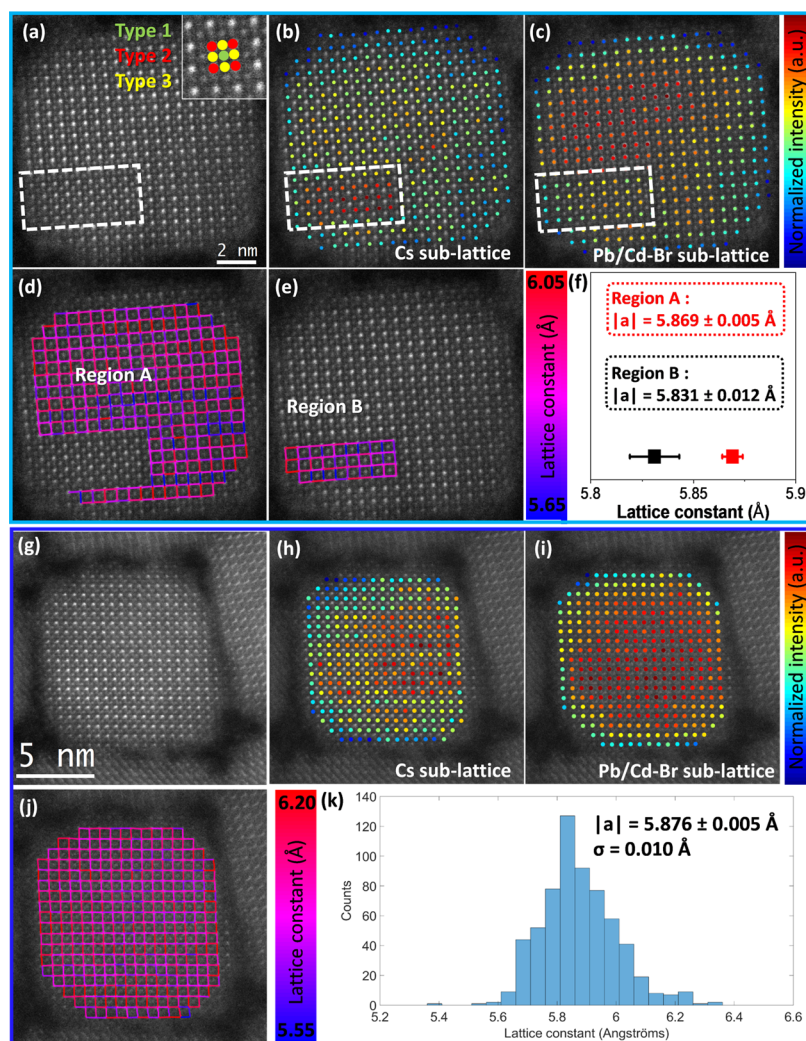
Figure 3. HAADF-STEM analysis of freshly prepared pristine $CsCd_{0.25}Pb_{0.75}Br_3$ NCs (a−f) and after DDABr exchange (g−j). (a) Typical high-resolution HAADF-STEM image of pristine NCs. Panels (b) and (c) show the normalized Gaussian peak volumes of Cs and Pb/Cd-Br sublattice columns of NCs reported in panel (a), respectively. The RP phase is enclosed in the white dashed rectangle. Panels (d) and (e) represent the neighbor column distance mapping of Pb/Cd-Br sublattice in the perovskite region (region A) and the RP phase region (region B) of corresponding NCs. (f) Mean lattice distribution of regions A and B. (g) Typical high-resolution HAADF-STEM image of DDABr-exchanged NCs. Panels (h) and (i) show the normalized Gaussian volumes of Cs and Pb/Cd-Br columns of NCs reported in panel (g), respectively. (j) Neighbor column distances mapping of type 1 sublattice of DDABr-exchanged NCs and (k) lattice parameter distribution of corresponding NCs. Note that the intensity scales are independent and normalized in panels (b), (c), (h), and (i).

These trends, overall, confirm the exchange of Cs-oleate with DDABr ligands on the surface of NCs.

We also carried out XRPD analyses of the pristine and DDABr-exchanged NCs, for both the freshly prepared samples and the same samples aged for 14 days. The relevant data are seen in Figure 2e (the corresponding patterns without background subtraction of both fresh and aged samples are reported in Figures S15 and S16, respectively). The XRPD patterns of the fresh samples both closely matched the cubic perovskite phase, in contrast with the orthorhombic phase of the pure $CsPbBr_3$ NCs. The slight shift of the XRPD peaks to higher angles compared to the reference $CsPbBr_3$ pattern (reference code: 98-018-1287) indicates a decrease in the cell volume, due to the partial substitution of lead with cadmium. Over aging, the DDABr-exchanged sample remained nearly unchanged, while the pristine sample evidenced a shift of peaks toward lower angles confirming the expansion in cell volume, which we ascribed to the loss of Cd^{2+} ions (the details are

discussed later in the electron microscopy section of aged NCs). Furthermore, the emergence of additional diffraction peaks upon aging in the pristine sample at around 24, 25, and 28 2-theta (conforming to the orthorhombic phase of $CsPbBr_3$) suggests the change in the crystal structure from cubic to orthorhombic (see the inset of the XRPD pattern for the aged pristine sample in Figure 2e, magnified 10 times). The loss of a substantial fraction of Cd^{2+} ions in the aged pristine sample, and obviously of a fraction of Br^- ions to maintain charge neutrality in NCs, was also corroborated by a decrease in the average size of the NCs (by TEM analysis) from 12.1 ± 1.4 nm in the fresh pristine sample to 11.2 ± 1.9 in the aged pristine sample (Figure S17).

We then proceeded to investigate the crystal structures of pristine NCs and of the corresponding NCs after various ligand-exchange procedures through quantitative high-resolution HAADF-STEM imaging. We first discuss in detail the two cases of the pristine and of the DDABr-exchanged samples
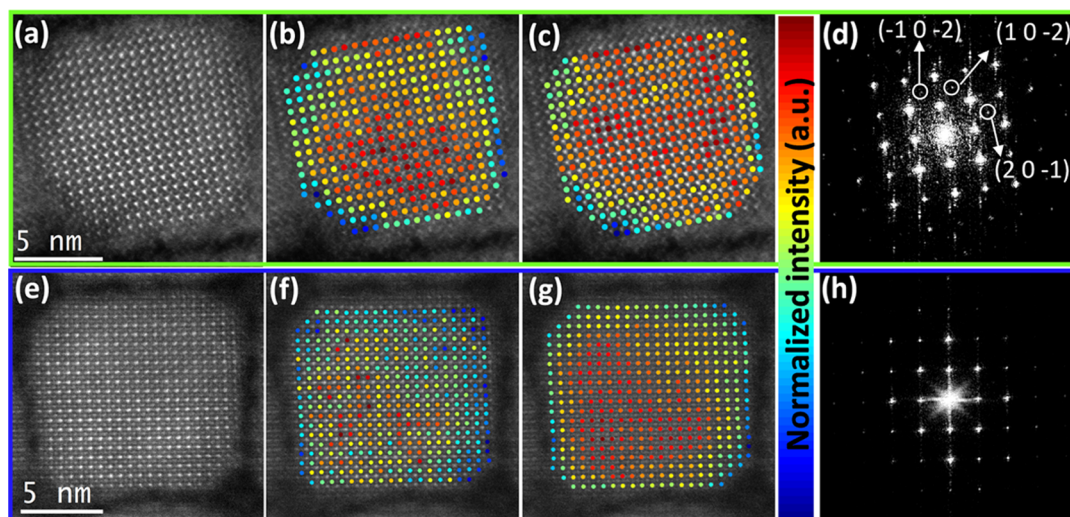
Figure 4. (a) Typical high-resolution HAADF-STEM image of a pristine NC after 6 days of aging. The intensities of type 1 and type 2 sublattices are depicted in panels (b) and (c), respectively. (d) Fourier transform of the nanocrystal shown in (a). The specific spots corresponding to orthorhombic $CsPbBr_3$ in [010] orientation are highlighted by white circles. (e) Representative DDABr-exchanged NCs after 10 days of aging. The column intensities of type 1 and type 2 sublattices are depicted in panels (f) and (g), respectively. (h) Fourier transform of the NCs shown in (e), corresponding to a cubic $CsPbBr_3$ in [100] orientation. The intensity scales of column intensities in panels (b), (c), (f), and (g) are independent and normalized.

(both freshly prepared and aged), as those two samples are the most diverging ones in terms of emission color stability, as discussed above. The corresponding analyses of the other samples are reported in the SI and are briefly discussed at the end of this section. Figure 3a shows a typical image of a fresh pristine NC. Since the HAADF-STEM signal approximately scales with the square of the atomic number Z, three atomic column types with different brightnesses could be distinguished outside the dashed white region (see inset of Figure 3a): type 1 corresponds to pure Cs columns ($Z_{Cs} = 55$), type 2 to Pb/Cd-Br columns ($Z_{Pb} = 82$, $Z_{Cd} = 48$, $Z_{Br} = 35$); and type 3 to Br columns.[31] The type 3 columns are hardly visible due to their relatively lower atomic number Z. The Fourier transform (FT) of this region (see Figure S18) corresponds to a metal halide perovskite cubic structure imaged along the [100] zone axis. Unlike in standard $CsPbBr_3$ NCs, we additionally observed several other regions, like the one inside the white dashed rectangle indicated in Figure 3a (see also Figures S19 and S20 for additional examples). Here, the differences in intensities for the different atomic columns are smaller. Moreover, the intensities appear higher (lower) in comparison to the type 1(2) columns for the $CsPbBr_3$ cubic structure.

To investigate this intensity difference in more detail, we measured the total scattered intensities of both types of columns in NCs using the StatSTEM software.[59] In this analysis, the columns were modeled as a superposition of Gaussian functions. The unknown model parameters, including the location and total scattered intensity, were estimated for each atomic column. The results, shown in Figure 3b,c for the type 1 and 2 sublattice columns, respectively, confirm the intensity difference of the atomic columns within and outside the dashed white region (see also Figure S20 for the same analysis of another NC). More precisely, columns corresponding purely to Cs in the $CsPbBr_3$ cubic structure showed an increase in intensity in the region contained in the white dashed rectangle, whereas columns expected to correspond to the Pb/Cd-Br type showed a reduction of intensity inside the

same region. These observations suggest different compositions of the atomic columns in the dashed white region in comparison to conventional perovskite phases. This is usually the signature of a Ruddlesden−Popper phase (RP).[71,72] A RP phase consists of n cubic perovskite layers separated by a [CsBr] layer, where n is an integer. This leads to a drastic change in the column compositions that mix both type 1 and 2 columns into one column. Our modeling of the corresponding RP and perovskite crystal lattices (see also the computations section later) indicates that if the Cd^{2+} and Pb^{2+} ions were homogeneously distributed throughout the NCs, there would be no difference in the lattice parameter between the RP domains and the other regions of the NCs, which adopt the cubic perovskite phase. However, the experimentally measured lattice parameter (i.e., the mean value of the column-to-column distance from the same sublattice) in these RP regions (5.831 ± 0.012 Å) is significantly smaller than the mean value in the rest of the NCs (5.869 ± 0.005 Å), where the error bar corresponds to the standard deviation on the mean value (see also Figure S21 for the lattice constant distribution of the two phases). This is also confirmed by a statistical Student's t-test[31] for the comparison of two mean values (see Figures 3d−f and S20). These results based on theoretical predictions (see later) suggest that the Cd/Pb ratio was higher here than in the rest of the NCs, suggesting that Cd^{2+} ions preferentially segregated in the RP regions leading to a lattice contraction. We then performed a similar quantitative analysis on the DDABr-exchanged NCs. The relevant data are displayed in Figure 3g; no RP phases were observed for these NCs. This was confirmed by the rather homogenous intensity distribution over the whole NCs of both type 1 and type 2 column sublattices, which are shown in Figure 3h,i, respectively, as the rather narrow distribution of the column-to-column distance of type 2 (see Figure 3j). The mean lattice parameter (MLP) measured for this NC equals 5.876 ± 0.005 Å (Figure 3k). Hence, it appears that the exchange with DDABr caused the transition of the RP domains to the cubic perovskite phase.

We then analyzed both samples after aging. Figure 4a–h shows the HAADF-STEM analysis of aged pristine and aged DDABr-exchanged NCs, respectively. Remarkably, in the pristine sample aged for 6 days, the RP phases had disappeared (Figures 4a and S22), which is confirmed by the relatively homogenous distribution of column intensities of type 1 (Figure 4c) and type 2 (Figure 4d). Such structural evolution upon aging, also backed by the corresponding optical features of the fresh and aged samples, as previously discussed (Figure 2), appears to be a direct consequence of the loss of Cd^{2+} ions from the NCs. In addition, the FT of the NC of Figure 4a, reported in Figure 4d, evidences the presence of specific planes corresponding to the orthorhombic phase of $CsPbBr_3$, testifying a transition from cubic to orthorhombic structure accompanying the loss of Cd^{2+}. This was further supported by STEM-EDX analysis of the aged pristine sample, which revealed a 7% content of Cd, down from 25% of the fresh pristine sample (Table S4). On the other hand, Figure 4e–h are images of a DDABr exchanged NC after 10 days of aging. No significant structural differences were observed when compared to the fresh DDABr exchanged NC sample (Figure 3g–k). The quantitative analyses of the column intensities of type 1 and 2, presented in Figure 4f–g are similar to the ones of the corresponding fresh sample, reported in Figure 3g–k. The lattice constant distribution (Figure S23) indicates a mean lattice of 5.888 ± 0.006 Å. According to the Student's *t*-test, there is no significant difference in mean lattice distance between the fresh and aged DDABr exchanged NCs. This is a strong indication that in the DDABr exchanged NCs, the Cd^{2+} ions were retained in the NCs more efficiently than in the pristine NCs.

We also performed similar analyses on the NCs exchanged with other ligands (Cs-oleate, Cs-PhAce, OLABr, PhEABr) and noticed a much lower occurrence of the RP phase already in the freshly exchanged samples (see Figure S24). As an example, we checked carefully the HAADF-STEM images acquired on both pristine and on NCs exchanged with Cs-oleate. We found that 63% of pristine NCs evidenced RP phases, while in the Cs-oleate-exchanged NCs the occurrence of the RP phases was reduced to 14%. This evidence suggests that any of the ligand-exchange procedures tested were harsh enough for the NCs to accelerate the transformation of the RP phases to cubic perovskite phases. However, when crossing these data with the various analyses discussed earlier, we can conclude that no surface treatment was as efficient as the DDABr treatment in preventing the escape of Cd^{2+} ions from NCs.

To understand with atomistic detail the structure and optoelectronic behavior of the $CsCd_xPb_{1-x}Br_3$ NCs prepared and analyzed in this work, we also performed density functional theory (DFT) calculations. At first, we looked at the origin of the blue shift that the system with mixed Pb/Cd composition experiences compared to the pure $CsPbBr_3$ NCs. To this aim, we computed the band structure for the orthorhombic (*Pnma*) $CsPbBr_3$ NCs at the DFT/PBE + SOC (SOC, spin−orbit coupling) level of theory, as shown in Figure 5a. The band gap is computed at 1.0 eV and is underestimated against the experiment, as is expected for the pure exchange−correlation functional such as PBE. Our goal, however, is to look at the effect of adding Cd to the lattice rather than in the absolute band gap, an effect that is captured by this level of theory. We computed the band structure for a 2 × 2 × 2 cubic $CsPbBr_3$ lattice, where one-fourth of the Pb
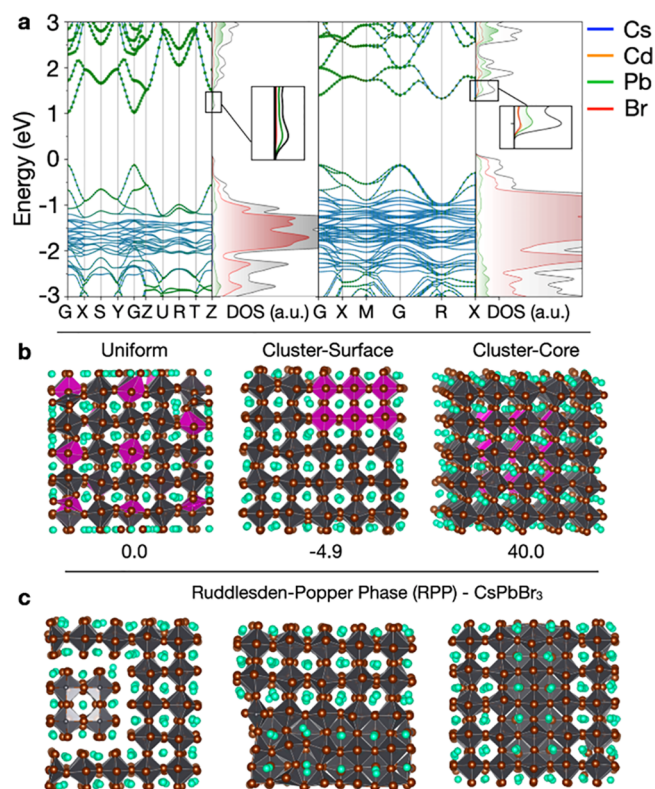
Figure 5. (a) Band structure of $CsPbBr_3$ (left) and alloyed $CsCd_{0.25}Pb_{0.75}Br_3$ (right) systems. The former was computed on a 1 × 1 × 1 unit cell, whereas the latter was computed on a cubic 2 × 2 × 2 cell with one-quarter of the metal atoms as Cd and the rest as Pb. (b) Cluster calculation of three types of stoichiometric alloyed NCs with a different distribution of the Cd atoms (25% in total) inside the lattice. The numbers below each system are the relative energies in kcal/mol versus the uniform distribution that is taken as reference. (c) NC model of the alloyed $CsCd_{0.25}Pb_{0.75}Br_3$ exhibiting the RP phase from three different orientations. All calculations of (a−c) were computed at the DFT/PBE level of theory.

atoms has been replaced by Cd, thus obtaining a 75:25% Pb/Cd composition, in line with the experiments. The band structure in Figure 5a (right side) shows that the gap widens to 1.44 eV and it becomes slightly indirect with the lowest transition occurring from a Gamma (G) to an R point. This indirect transition explains in part the worsening of the optoelectronic characteristics of the material in terms of PLQYs. The indirect nature of the band gap is also reflected in the increased PL lifetime at increasing concentration of Cd in the sample (Figure S8 and Table S2). The opening of the gap is in line with what is observed in the experiments and is characterized by a less dispersive conduction band minimum at the G point, which is shifted higher in energy, followed by a strong stabilization of the band at the R point emerging from the bonding orbital overlap of the empty 5s orbitals of Cd with the unoccupied 6p of Pb. Overall, both effects lead to a gap opening.

Besides this, we built and computed also explicit NC models of mixed $CsCd_{0.25}Pb_{0.75}Br_3$ NCs to understand how Cd and Pb are distributed inside the lattice. Since the number of possible combinations is enormous, we focused on three types of configurations: a uniform distribution of Cd^{2+} and Pb^{2+} ions inside the lattice; a cluster configuration where Cd^{2+} ions are segregated at the surface and finally another cluster

configuration where all of the Cd^{2+} ions are segregated at the core (Figure 5b). The main result is that a Cd clusterization in the core region of the NCs is energetically very unfavorable, whereas the Cd^{2+} ions appear either to be distributed uniformly across the NCs or to segregate at the surface. It is likely (although we have no further supporting ground for this hypothesis) that surface segregation of Cd^{2+} ions can favor the local formation of an RP phase bordering the surface of the NCs and rarely entirely embedded in the NCs, as revealed by our electron microscopy analysis. To better understand this aspect, we also computed the geometry and electronic structure of an NC model system that exhibits the RP phase. As shown in Figure 5c for the pure "pervoskite-$CsPbBr_3$/RP-$CsPbBr_3$" NCs and in the SI for the "pervoskite-$CsCd_xPb_{1-x}Br_3$/RP-$CsCd_xPb_{1-x}Br_3$" NCs, the RP phases are stable from the computational point of view and their electronic structures are substantially similar to those of the pure perovskite phase, albeit with the additional presence of localized states at the interface, another point that adds to the loss of the PLQY of the native NCs compared to the pure $CsPbBr_3$ NCs. Even more interestingly, we noted that the presence of the RP phase by itself is not sufficient to explain the lattice contraction in the RP region observed in the TEM images. The analysis of the Pb–Pb bond distance in the DFT calculations indeed shows that this remains the same in both phases (see Figure S25). On the other hand, when we modeled a preferential accumulation of Cd in the RP phase and then analyzed the Cd–Cd distances, we noticed a contraction of the lattice in the RP region that is comparable to what was observed experimentally by electron microscopy.

As for the statistical significance of the RP phases in our samples, we sought to identify their eventual presence in the experimental XRPD patterns. To do so, we had to calculate an XRPD pattern of an "ideal" Cs_2PbBr_4 RP phase first. Such phase was modeled by starting from the $Cs_2PbI_2Cl_2$ phase reported by Li et al.,[73] and replacing iodine and chlorine atoms in the structure with bromine atoms, followed by relaxation of a $2 \times 2 \times 2$ cell for both atomic positions and cell parameters by DFT/PBE calculations. The simulated XRPD pattern, reported in Figure S26 of the SI, is compared with that of bulk cubic $CsPbBr_3$ and that of $CsCd_{0.25}Pb_{0.75}Br_3$ NCs. As can be seen from the comparison, the only significantly distinctive peak for Cs_2PbBr_4 is at around 9-10 °, as the other peaks are either low in intensity or they overlap with those of the cubic perovskite phase. Alloying with Cd should move this low-angle peak to higher angles and decrease its relative intensity. Although all our previous XRPD patterns had been collected starting from 10° in 2Θ, XRPD patterns on freshly prepared pristine Cs-oleate-coated samples, collected from 7°, did not exhibit such low-angle peaks. Our conclusion is that these RP phases have a low statistical significance in our samples, and additionally, the RP domains, when present, are small and should contribute with considerable broadened peaks.

The experimental and theoretical data that we have presented above allow us to draw a solid hypothesis on the overall optical/structural stability of the NCs and their evolution depending on the type of surface passivation. We expect that mixing lead and cadmium precursors at the synthesis stage leads to the formation of the RP phases already during the nucleation and growth of the Cs-oleate-capped NCs. The formation of the RP phases is most likely driven by the difference in ionic radii of Cd^{2+} and Pb^{2+} cations, and probably, these are kinetically trapped configurations.

In the NCs, Cd is distributed homogenously inside the perovskite phase, albeit with a slight accumulation in the RP phase. Overall, the symmetry of the structure is closer to the cubic than to the orthorhombic one (the latter typical of the pure $CsPbBr_3$ composition), and the band gap shifts to the blue region, as also evidenced by DFT calculations. When left untreated, the Cs-oleate-coated NCs evolve by expelling a considerable fraction of the Cd^{2+} ions through a concomitant loss of loosely bound Cs(oleate) and Cd(oleate)$_2$ species, and a structural reorganization of the RP domains into perovskite ones. By doing so, the overall optical features of the NCs evolve toward those of the pure, green emissive $CsPbBr_3$ NCs. The expulsion of Cd^{2+} ions is compatible with the fact that the octahedral coordination is not their preferred one. The various ligand-exchange treatments, on the other hand, accelerate the RP to perovskite transition, a process that is presumably triggered at the surface. Following this transition, the Cd^{2+} ions become homogenously re-distributed throughout the NC lattice. On the other hand, the various ligand-exchange treatments have different efficacies in preventing the loss of Cd^{2+} ions from the NCs: the treatments with Cs-carboxylate ligands are less successful in preventing such loss, while those with ammonium bromide ligands are more successful, especially the one with DDABr. Hence, we conclude that the latter ligands are the most efficient in saturating surface vacancies, which are most likely the channels through which Cd^{2+} ions could escape from the NCs. In this case, the band gap is retained in the blue, even after aging, and the optimal surface passivation helps to preserve the PLQYs at values around 40%. Yet, the slightly indirect band gap nature of the lowest energy transition possibly precludes a further enhancement of the PLQYs to the values typical of the pure $CsPbBr_3$ composition.

Finally, we fabricated light-emitting diodes (LEDs) to verify the stability in the electroluminescence (EL) of a film of DDABr exchanged $CsCd_{0.25}Pb_{0.75}Br_3$ NCs. Details on LED fabrication and device structure are reported in the Experimental Section and in Figure S27a, respectively. A typical LED, under constant applied bias (4 V, Figure S27b), featured an EL spectrum centered at 480 nm, i.e., slightly red-shifted from the PL of the colloidal dispersion (476 nm). The emission did not vary significantly under device operation over 3 min, again supporting the structural stability of the DDABr-exchanged NCs. The luminance–voltage–current density and the external quantum efficiency curves of a typical LED are reported in Figures S28 and S29.

■ CONCLUSIONS

We have shown that the structural and spectral stability of mixed cation perovskite NCs strongly depends on their surface passivation. Combined experimental and theoretical investigations reveal that Cs-oleate-capped $CsCd_{0.25}Pb_{0.75}Br_3$ NCs are characterized by Cd-segregated RP phases in addition to the perovskite phase. At this stage, it is not clear to us how these phases can be eliminated at the synthesis stage; most likely, a different choice of surfactants might affect their formation, and this will be the subject of future investigations. This structural heterogeneity can be removed by treating the NCs with various ligands postsynthesis or by simply aging, although in most of these cases their emission color is unstable due to the expulsion of Cd^{2+} ions. Among the various postsynthesis ligand-exchange strategies, we found that the ones employing ammonium bromides, and especially DDABr,

suppress the out-diffusion of Cd^{2+} ions. In this case, the NCs tend to retain their blue emission over time, both in colloidal dispersions and in electroluminescent devices, as well as their cubic phase. Although we succeed to obtain stable alloys, pure blue emission (i.e., centered at 460−470 nm) remains unattainable with our NCs, even with those having the highest content of Cd^{2+} cations. One possible development in this direction might rely on the synthesis of quantum confined $CsCd_xPb_{1-x}Br_3$ alloy NCs. This work highlights the critical role of surface passivation on the structural and optical properties of mixed cation halide perovskite NCs and should be generalized to study the effect of different types of ligand passivation on the stability of other halide perovskite alloy compositions.

ASSOCIATED CONTENT

Ⓢ Supporting Information

The Supporting Information is available free of charge at https://pubs.acs.org/doi/10.1021/acs.chemmater.0c03825.

Results of various surface treatments such as TEM images, optical absorption, PL, PLQY, and PL lifetimes, XRPD patterns, EDS compositional analysis, HR-TEM/STEM images, XPS, NMR spectra (^{1}H, and [1]H-NOESY), and computational analysis (PDF)

AUTHOR INFORMATION

Corresponding Authors

Muhammad Imran − Nanochemistry Department, Istituto Italiano di Tecnologia (IIT), 16163 Genova, Italy; ⓞ orcid.org/0000-0001-7091-6514; Email: muhammad.imran@iit.it

Ivan Infante − Nanochemistry Department, Istituto Italiano di Tecnologia (IIT), 16163 Genova, Italy; Department of Theoretical Chemistry, Faculty of Science, Vrije Universiteit Amsterdam, 1081 HV Amsterdam, The Netherlands; ⓞ orcid.org/0000-0003-3467-9376; Email: ivan.infante@iit.it

Sara Bals − Electron Microscopy for Materials Science (EMAT) and NANOlab Center of Excellence, University of Antwerp, 2020 Antwerp, Belgium; ⓞ orcid.org/0000-0002-4249-8017; Email: sara.bals@uantwerpen.be

Liberato Manna − Nanochemistry Department, Istituto Italiano di Tecnologia (IIT), 16163 Genova, Italy; ⓞ orcid.org/0000-0003-4386-7985; Email: liberato.manna@iit.it

Authors

Julien Ramade − Electron Microscopy for Materials Science (EMAT) and NANOlab Center of Excellence, University of Antwerp, 2020 Antwerp, Belgium

Francesco Di Stasio − Photonic Nanomaterials Lab, Istituto Italiano di Tecnologia (IIT), 16163 Genova, Italy; ⓞ orcid.org/0000-0002-2079-3322

Manuela De Franco − Dipartimento di Chimica e Chimica Industriale, Università degli Studi di Genova, 16146 Genova, Italy

Joka Buha − Nanochemistry Department, Istituto Italiano di Tecnologia (IIT), 16163 Genova, Italy

Sandra Van Aert − Electron Microscopy for Materials Science (EMAT) and NANOlab Center of Excellence, University of Antwerp, 2020 Antwerp, Belgium

Luca Goldoni − Analytical Chemistry Lab, Istituto Italiano di Tecnologia (IIT), 16163 Genova, Italy

Simone Lauciello − Electron Microscopy Facility, Istituto Italiano di Tecnologia (IIT), 16163 Genova, Italy

Mirko Prato − Materials Characterization Facility, Istituto Italiano di Tecnologia (IIT), 16163 Genova, Italy; ⓞ orcid.org/0000-0002-2188-8059

Complete contact information is available at:
https://pubs.acs.org/10.1021/acs.chemmater.0c03825

Notes

The authors declare no competing financial interest.

ACKNOWLEDGMENTS

REFERENCES

(1) Kovalenko, M. V.; Protesescu, L.; Bodnarchuk, M. I. Properties and potential optoelectronic applications of lead halide perovskite nanocrystals. Science 2017, 358, 745−750.

(2) Quan, L. N.; Rand, B. P.; Friend, R. H.; Mhaisalkar, S. G.; Lee, T.-W.; Sargent, E. H. Perovskites for Next-Generation Optical Sources. Chem. Rev. 2019, 119, 7444−7477.

(3) Huang, H.; Polavarapu, L.; Sichert, J. A.; Susha, A. S.; Urban, A. S.; Rogach, A. L. Colloidal lead halide perovskite nanocrystals: synthesis, optical properties and applications. NPG Asia Mater. 2016, 8, e328.

(4) Yang, D.; Li, X.; Zeng, H. Surface Chemistry of All Inorganic Halide Perovskite Nanocrystals: Passivation Mechanism and Stability. Adv. Mater. Interfaces 2018, 5, No. 1701662.

(5) Zheng, X.; Hou, Y.; Sun, H.-T.; Mohammed, O. F.; Sargent, E. H.; Bakr, O. M. Reducing Defects in Halide Perovskite Nanocrystals for Light-Emitting Applications. J. Phys. Chem. Lett. 2019, 10, 2629−2640.

(6) Fu, Y.; Zhu, H.; Chen, J.; Hautzinger, M. P.; Zhu, X.-Y.; Jin, S. Metal halide perovskite nanostructures for optoelectronic applications and the study of physical properties. Nat. Rev. Mater. 2019, 4, 169−188.

(7) Protesescu, L.; Yakunin, S.; Bodnarchuk, M. I.; Krieg, F.; Caputo, R.; Hendon, C. H.; Yang, R. X.; Walsh, A.; Kovalenko, M. V. Nanocrystals of Cesium Lead Halide Perovskites ($CsPbX_3$, X = Cl, Br, and I): Novel Optoelectronic Materials Showing Bright Emission with Wide Color Gamut. Nano Lett. 2015, 15, 3692−3696.

(8) Nedelcu, G.; Protesescu, L.; Yakunin, S.; Bodnarchuk, M. I.; Grotevent, M. J.; Kovalenko, M. V. Fast anion-exchange in highly luminescent nanocrystals of cesium lead halide perovskites ($CsPbX_3$, X = Cl, Br, I). Nano Lett. 2015, 15, 5635−5640.

(9) Akkerman, Q. A.; D'Innocenzo, V.; Accornero, S.; Scarpellini, A.; Petrozza, A.; Prato, M.; Manna, L. Tuning the optical properties of cesium lead halide perovskite nanocrystals by anion exchange reactions. J. Am. Chem. Soc. 2015, 137, 10276−10281.

(10) Dong, Y.; Qiao, T.; Kim, D.; Parobek, D.; Rossi, D.; Son, D. H. Precise control of quantum confinement in cesium lead halide perovskite quantum dots via thermodynamic equilibrium. Nano Lett. 2018, 18, 3716−3722.

(11) Lu, C.-H.; Biesold-McGee, G. V.; Liu, Y.; Kang, Z.; Lin, Z. Doping and ion substitution in colloidal metal halide perovskite nanocrystals. *Chem. Soc. Rev.* 2020, 49, 4953−5007.

(12) Chen, Y.; Liu, Y.; Hong, M. Cation-Doping Matters in Caesium Lead Halide Perovskite Nanocrystals: from Physicochemical Fundamentals to Optoelectronic Applications. *Nanoscale* 2020, 12, 12228−12248.

(13) Swarnkar, A.; Mir, W. J.; Nag, A. Can B-site doping or alloying improve thermal-and phase-stability of all-inorganic CsPbX$_3$ (X = Cl, Br, I) perovskites? *ACS Energy Lett.* 2018, 3, 286−289.

(14) Guo, J.; Fu, Y.; Lu, M.; Zhang, X.; Kershaw, S. V.; Zhang, J.; Luo, S.; Li, Y.; Yu, W. W.; Rogach, A. L.; et al. Cd-Rich Alloyed CsPb$_{1-x}$Cd$_x$Br$_3$ Perovskite Nanorods with Tunable Blue Emission and Fermi Levels Fabricated through Crystal Phase Engineering. *Adv. Sci.* 2020, 7, No. 2000930.

(15) Suri, M.; Hazarika, A.; Larson, B. W.; Zhao, Q.; Vallés-Pelarda, M.; Siegler, T. D.; Abney, M. K.; Ferguson, A. J.; Korgel, B. A.; Luther, J. M. Enhanced Open-Circuit Voltage of Wide-Bandgap Perovskite Photovoltaics by Using Alloyed (FA$_{1-x}$Cs$_x$)Pb(I$_{1-x}$Br$_x$)$_3$ Quantum Dots. *ACS Energy Lett.* 2019, 4, 1954−1960.

(16) Mondal, N.; De, A.; Samanta, A. Achieving near-unity photoluminescence efficiency for blue-violet-emitting perovskite nanocrystals. *ACS Energy Lett.* 2019, 4, 32−39.

(17) Akkerman, Q. A.; Martínez-Sarti, L.; Goldoni, L.; Imran, M.; Baranov, D.; Bolink, H. J.; Palazon, F.; Manna, L. Molecular Iodine for a General Synthesis of Binary and Ternary Inorganic and Hybrid Organic−Inorganic Iodide Nanocrystals. *Chem. Mater.* 2018, 30, 6915−6921.

(18) Bi, C.; Sun, X.; Huang, X.; Wang, S.; Yuan, J.; Wang, J. X.; Pullerits, T.; Tian, J. Stable CsPb$_{1-x}$Zn$_x$I$_3$ colloidal quantum dots with ultralow density of trap states for high performance solar cells. *Chem. Mater.* 2020, 32, 6105−6113.

(19) Liu, F.; Zhang, Y.; Ding, C.; Kawabata, K.; Yoshihara, Y.; Toyoda, T.; Hayase, S.; Minemoto, T.; Wang, R.; Shen, Q. Trioctylphosphine Oxide Acts as Alkahest for SnX$_2$/PbX$_2$: A General Synthetic Route to Perovskite ASn$_x$Pb$_{1-x}$X$_3$ (A = Cs, FA, MA; X = Cl, Br, I) Quantum Dots. *Chem. Mater.* 2020, 32, 1089−1100.

(20) Gualdrón-Reyes, A. F.; Yoon, S. J.; Barea, E. M.; Agouram, S.; Muñoz-Sanjosé, V.; Meléndez, Á. M.; Niño-Gómez, M. E.; Mora-Seró, I. Controlling the phase segregation in mixed halide perovskites through nanocrystal size. *ACS Energy Lett.* 2018, 4, 54−62.

(21) Dahl, J.; Wang, X.; Huang, X.; Chan, E.; Alivisatos, A. P. Elucidating the weakly reversible Cs-Pb-Br perovskite nanocrystal reaction network with high-throughput maps and transformations. *J. Am. Chem. Soc.* 2020, 142, 11915−11926.

(22) Sichert, J. A.; Tong, Y.; Mutz, N.; Vollmer, M.; Fischer, S.; Milowska, K. Z.; García Cortadella, R.; Nickel, B.; Cardenas-Daw, C.; Stolarczyk, J. K.; et al. Quantum size effect in organometal halide perovskite nanoplatelets. *Nano Lett.* 2015, 15, 6521−6527.

(23) Bekenstein, Y.; Koscher, B. A.; Eaton, S. W.; Yang, P.; Alivisatos, A. P. Highly luminescent colloidal nanoplates of perovskite cesium lead halide and their oriented assemblies. *J. Am. Chem. Soc.* 2015, 137, 16008−16011.

(24) Sun, S.; Yuan, D.; Xu, Y.; Wang, A.; Deng, Z. Ligand-mediated synthesis of shape-controlled cesium lead halide perovskite nanocrystals via reprecipitation process at room temperature. *ACS Nano* 2016, 10, 3648−3657.

(25) Imran, M.; Caligiuri, V.; Wang, M.; Goldoni, L.; Prato, M.; Krahne, R.; De Trizio, L.; Manna, L. Benzoyl halides as alternative precursors for the colloidal synthesis of lead-based halide perovskite nanocrystals. *J. Am. Chem. Soc.* 2018, 140, 2656−2664.

(26) Xu, L.; Yuan, S.; Zeng, H.; Song, J. A comprehensive review of doping in perovskite nanocrystals/quantum dots: evolution of structure, electronics, optics, and light-emitting diodes. *Mater. Today Nano* 2019, 6, No. 100036.

(27) Li, X.; Wu, Y.; Zhang, S.; Cai, B.; Gu, Y.; Song, J.; Zeng, H. CsPbX$_3$ quantum dots for lighting and displays: room-temperature synthesis, photoluminescence superiorities, underlying origins and white light-emitting diodes. *Adv. Funct. Mater.* 2016, 26, 2435−2445.

(28) Bohn, B. J.; Tong, Y.; Gramlich, M.; Lai, M. L.; Döblinger, M.; Wang, K.; Hoye, R. L.; Müller-Buschbaum, P.; Stranks, S. D.; Urban, A. S.; et al. Boosting tunable blue luminescence of halide perovskite nanoplatelets through postsynthetic surface trap repair. *Nano Lett.* 2018, 18, 5231−5238.

(29) Protesescu, L.; Yakunin, S.; Kumar, S.; Bär, J.; Bertolotti, F.; Masciocchi, N.; Guagliardi, A.; Grotevent, M.; Shorubalko, I.; Bodnarchuk, M. I.; et al. Dismantling the "red wall" of colloidal perovskites: highly luminescent formamidinium and formamidinium−cesium lead iodide nanocrystals. *ACS Nano* 2017, 11, 3119−3134.

(30) Hautzinger, M. P.; Pan, D.; Pigg, A. K.; Fu, Y.; Morrow, D. J.; Leng, M.; Kuo, M.-Y.; Spitha, N.; Lafayette, D. P.; Kohler, D. D.; et al. Band Edge Tuning of Two-Dimensional Ruddlesden−Popper Perovskites by A Cation Size Revealed through Nanoplates. *ACS Energy Lett.* 2020, 5, 1430−1437.

(31) Van der Stam, W.; Geuchies, J. J.; Altantzis, T.; Van Den Bos, K. H.; Meeldijk, J. D.; Van Aert, S.; Bals, S.; Vanmaekelbergh, D.; de Mello Donega, C. Highly Emissive Divalent-Ion-Doped Colloidal CsPb$_{1-x}$M$_x$Br$_3$ Perovskite Nanocrystals through Cation Exchange. *J. Am. Chem. Soc.* 2017, 139, 4087−4097.

(32) Dunlap-Shohl, W. A.; Younts, R.; Gautam, B.; Gundogdu, K.; Mitzi, D. B. Effects of Cd diffusion and doping in high-performance perovskite solar cells using CdS as electron transport layer. *J. Phys. Chem. C* 2016, 120, 16437−16445.

(33) Cai, T.; Yang, H.; Hills-Kimball, K.; Song, J.-P.; Zhu, H.; Hofman, E.; Zheng, W.; Rubenstein, B. M.; Chen, O. Synthesis of all-inorganic Cd-doped CsPbCl$_3$ perovskite nanocrystals with dual-wavelength emission. *J. Phys. Chem. Lett.* 2018, 9, 7079−7084.

(34) Ijaz, P.; Imran, M.; Soares, M. M.; Tolentino, H. C.; Martín-García, B.; Giannini, C.; Moreels, I.; Manna, L.; Krahne, R. Composition-, size-, and surface functionalization-dependent optical properties of lead bromide perovskite nanocrystals. *J. Phys. Chem. Lett.* 2020, 11, 2079−2085.

(35) Murray, C.; Norris, D. J.; Bawendi, M. G. Synthesis and characterization of nearly monodisperse CdE (E = sulfur, selenium, tellurium) semiconductor nanocrystallites. *J. Am. Chem. Soc.* 1993, 115, 8706−8715.

(36) Alivisatos, A. P. Semiconductor clusters, nanocrystals, and quantum dots. *Science* 1996, 271, 933−937.

(37) Polavarapu, L.; Nickel, B.; Feldmann, J.; Urban, A. S. Advances in Quantum-Confined Perovskite Nanocrystals for Optoelectronics. *Adv. Energy Mater.* 2017, 7, No. 1700267.

(38) Shamsi, J.; Rastogi, P.; Caligiuri, V.; Abdelhady, A. L.; Spirito, D.; Manna, L.; Krahne, R. Bright-emitting perovskite films by large-scale synthesis and photoinduced solid-state transformation of CsPbBr$_3$ nanoplatelets. *ACS Nano* 2017, 11, 10206−10213.

(39) Di Stasio, F.; Imran, M.; Akkerman, Q. A.; Prato, M.; Manna, L.; Krahne, R. Reversible Concentration-Dependent Photoluminescence Quenching and Change of Emission Color in CsPbBr$_3$ Nanowires and Nanoplatelets. *J. Phys. Chem. Lett.* 2017, 8, 2725−2729.

(40) Zhang, H.; Fu, X.; Tang, Y.; Wang, H.; Zhang, C.; William, W. Y.; Wang, X.; Zhang, Y.; Xiao, M. Phase segregation due to ion migration in all-inorganic mixed-halide perovskite nanocrystals. *Nat. Commun.* 2019, 10, No. 1088.

(41) Yoon, S. J.; Kuno, M.; Kamat, P. V. Shift happens. How halide ion defects influence photoinduced segregation in mixed halide perovskites. *ACS Energy Lett.* 2017, 2, 1507−1514.

(42) Correa-Baena, J.-P.; Luo, Y.; Brenner, T. M.; Snaider, J.; Sun, S.; Li, X.; Jensen, M. A.; Hartono, N. T. P.; Nienhaus, L.; Wieghold, S.; et al. Homogenized halides and alkali cation segregation in alloyed organic-inorganic perovskites. *Science* 2019, 363, 627−631.

(43) Brennan, M. C.; Ruth, A.; Kamat, P. V.; Kuno, M. Photoinduced Anion Segregation in Mixed Halide Perovskites. *Trends Chem.* 2020, 2, 282−301.

(44) Li, G.; Rivarola, F. W. R.; Davis, N. J.; Bai, S.; Jellicoe, T. C.; de la Peña, F.; Hou, S.; Ducati, C.; Gao, F.; Friend, R. H.; et al. Highly efficient perovskite nanocrystal light-emitting diodes enabled by a universal crosslinking method. *Adv. Mater.* 2016, 28, 3528−3534.

(45) Li, C.-H. A.; Zhou, Z.; Vashishtha, P.; Halpert, J. E. The Future Is Blue (LEDs): Why Chemistry Is the Key to Perovskite Displays. *Chem. Mater.* **2019**, *31*, 6003–6032.

(46) Shynkarenko, Y.; Bodnarchuk, M. I.; Bernasconi, C.; Berezovska, Y.; Verteletskyi, V.; Ochsenbein, S. T.; Kovalenko, M. V. Direct Synthesis of Quaternary Alkylammonium-Capped Perovskite Nanocrystals for Efficient Blue and Green Light-Emitting Diodes. *ACS Energy Lett.* **2019**, *4*, 2703–2711.

(47) Brennan, M. C.; Toso, S.; Pavlovetc, I. M.; Zhukovskyi, M.; Marras, S.; Kuno, M.; Manna, L.; Baranov, D. Superlattices are Greener on the Other Side: How Light Transforms Self-Assembled Mixed Halide Perovskite Nanocrystals. *ACS Energy Lett.* **2020**, *5*, 1465–1473.

(48) Ruan, S.; Surmiak, M.-A.; Ruan, Y.; McMeekin, D. P.; Ebendorff-Heidepriem, H.; Cheng, Y.-B.; Lu, J.; McNeill, C. R. Light induced degradation in mixed-halide perovskites. *J. Mater. Chem. C* **2019**, *7*, 9326–9334.

(49) Domanski, K.; Roose, B.; Matsui, T.; Saliba, M.; Turren-Cruz, S.-H.; Correa-Baena, J.-P.; Carmona, C. R.; Richardson, G.; Foster, J. M.; De Angelis, F.; et al. Migration of cations induces reversible performance losses over day/night cycling in perovskite solar cells. *Energy Environ. Sci.* **2017**, *10*, 604–613.

(50) Huang, J.; Xu, P.; Liu, J.; You, X. Z. Sequential Introduction of Cations Deriving Large-Grain $Cs_xFA_{1-x}PbI_3$ Thin Film for Planar Hybrid Solar Cells: Insight into Phase-Segregation and Thermal-Healing Behavior. *Small* **2017**, *13*, No. 1603225.

(51) Kubicki, D. J.; Prochowicz, D.; Hofstetter, A.; Zakeeruddin, S. M.; Grätzel, M.; Emsley, L. Phase segregation in potassium-doped lead halide perovskites from ^{39}K solid-state NMR at 21.1 T. *J. Am. Chem. Soc.* **2018**, *140*, 7232–7238.

(52) Paul, S.; Bladt, E.; Richter, A. F.; Döblinger, M.; Tong, Y.; Huang, H.; Dey, A.; Bals, S.; Debnath, T.; Polavarapu, L.; Feldmann, J. Manganese-Doping-Induced Quantum Confinement within Host Perovskite Nanocrystals through Ruddlesden–Popper Defects. *Angew. Chem., Int. Ed.* **2020**, *59*, 6794–6799.

(53) Saliba, M.; Matsui, T.; Domanski, K.; Seo, J.-Y.; Ummadisingu, A.; Zakeeruddin, S. M.; Correa-Baena, J.-P.; Tress, W. R.; Abate, A.; Hagfeldt, A.; Gratzel, M. Incorporation of rubidium cations into perovskite solar cells improves photovoltaic performance. *Science* **2016**, *354*, 206–209.

(54) Shao, Y.; Fang, Y.; Li, T.; Wang, Q.; Dong, Q.; Deng, Y.; Yuan, Y.; Wei, H.; Wang, M.; Gruverman, A.; et al. Grain boundary dominated ion migration in polycrystalline organic-inorganic halide perovskite films. *Energy Environ. Sci.* **2016**, *9*, 1752–1759.

(55) Abdi-Jalebi, M.; Andaji-Garmaroudi, Z.; Cacovich, S.; Stavrakas, C.; Philippe, B.; Richter, J. M.; Alsari, M.; Booker, E. P.; Hutter, E. M.; Pearson, A. J.; et al. Maximizing and stabilizing luminescence from halide perovskites with potassium passivation. *Nature* **2018**, *555*, 497–501.

(56) Zheng, X.; Hou, Y.; Bao, C.; Yin, J.; Yuan, F.; Huang, Z.; Song, K.; Liu, J.; Troughton, J.; Gasparini, N.; et al. Managing grains and interfaces via ligand anchoring enables 22.3%-efficiency inverted perovskite solar cells. *Nat. Energy* **2020**, *5*, 131–140.

(57) Hao, M.; Bai, Y.; Zeiske, S.; Ren, L.; Liu, J.; Yuan, Y.; Zarrabi, N.; Cheng, N.; Ghasemi, M.; Chen, P.; et al. Ligand-assisted cation-exchange engineering for high-efficiency colloidal $Cs_{1-x}FA_xPbI_3$ quantum dot solar cells with reduced phase segregation. *Nat. Energy* **2020**, *5*, 79–88.

(58) Imran, M.; Ijaz, P.; Baranov, D.; Goldoni, L.; Petralanda, U.; Akkerman, Q.; Abdelhady, A. L.; Prato, M.; Bianchini, P.; Infante, I.; Manna, L. Shape-Pure, Nearly Monodispersed $CsPbBr_3$ Nanocubes Prepared Using Secondary Aliphatic Amines. *Nano Lett.* **2018**, *18*, 7822–7831.

(59) De Backer, A.; Van den Bos, K.; Van den Broek, W.; Sijbers, J.; Van Aert, S. StatSTEM: an efficient approach for accurate and precise model-based quantification of atomic resolution electron microscopy images. *Ultramicroscopy* **2016**, *171*, 104–116.

(60) Wu, P. S.; Otting, G. Rapid pulse length determination in high-resolution NMR. *J. Magn. Reson.* **2005**, *176*, 115–119.

(61) Jeener, J.; Meier, B.; Bachmann, P.; Ernst, R. Investigation of exchange processes by two-dimensional NMR spectroscopy. *J. Chem. Phys.* **1979**, *71*, 4546–4553.

(62) Perdew, J. P.; Burke, K.; Ernzerhof, M. Generalized gradient approximation made simple. *Phys. Rev. Lett.* **1996**, *77*, 3865.

(63) Kresse, G.; Furthmüller, J. Efficient iterative schemes for ab initio total-energy calculations using a plane-wave basis set. *Phys. Rev. B* **1996**, *54*, 11169.

(64) Kresse, G.; Hafner, J. Ab initio molecular dynamics for liquid metals. *Phys. Rev. B* **1993**, *47*, 558.

(65) Hutter, J.; Iannuzzi, M.; Schiffmann, F.; VandeVondele, J. cp2k: atomistic simulations of condensed matter systems. *Wiley Interdiscip. Rev.: Comput. Mol. Sci.* **2014**, *4*, 15–25.

(66) Imran, M.; Ijaz, P.; Goldoni, L.; Maggioni, D.; Petralanda, U.; Prato, M.; Almeida, G.; Infante, I.; Manna, L. Simultaneous Cationic and Anionic Ligand Exchange For Colloidally Stable $CsPbBr_3$ Nanocrystals. *ACS Energy Lett.* **2019**, *4*, 819–824.

(67) De Roo, J.; Ibáñez, M.; Geiregat, P.; Nedelcu, G.; Walravens, W.; Maes, J.; Martins, J. C.; Van Driessche, I.; Kovalenko, M. V.; Hens, Z. Highly dynamic ligand binding and light absorption coefficient of cesium lead bromide perovskite nanocrystals. *ACS Nano* **2016**, *10*, 2071–2081.

(68) Nenon, D. P.; Pressler, K.; Kang, J.; Koscher, B. A.; Olshansky, J. H.; Osowiecki, W. T.; Koc, M. A.; Wang, L.-W.; Alivisatos, A. P. Design principles for trap-free $CsPbX_3$ nanocrystals: enumerating and eliminating surface halide vacancies with softer lewis bases. *J. Am. Chem. Soc.* **2018**, *140*, 17760–17772.

(69) Fritzinger, B.; Moreels, I.; Lommens, P.; Koole, R.; Hens, Z.; Martins, J. C. In situ observation of rapid ligand exchange in colloidal nanocrystal suspensions using transfer NOE nuclear magnetic resonance spectroscopy. *J. Am. Chem. Soc.* **2009**, *131*, 3024–3032.

(70) Chen, Y.; Smock, S. R.; Flintgruber, A. H.; Perras, F. A.; Brutchey, R. L.; Rossini, A. J. Surface Termination of $CsPbBr_3$ Perovskite Quantum Dots Determined by Solid-State NMR Spectroscopy. *J. Am. Chem. Soc.* **2020**, *142*, 6117–6127.

(71) Yu, Y.; Zhang, D.; Yang, P. Ruddlesden–Popper phase in two-dimensional inorganic halide perovskites: a plausible model and the supporting observations. *Nano Lett.* **2017**, *17*, 5489–5494.

(72) Akkerman, Q. A.; Bladt, E.; Petralanda, U.; Dang, Z.; Sartori, E.; Baranov, D.; Abdelhady, A. L.; Infante, I.; Bals, S.; Manna, L. Fully Inorganic Ruddlesden–Popper Double Cl–I and Triple Cl–Br–I Lead Halide Perovskite Nanocrystals. *Chem. Mater.* **2019**, *31*, 2182–2190.

(73) Li, J.; Yu, Q.; He, Y.; Stoumpos, C. C.; Niu, G.; Trimarchi, G. G.; Guo, H.; Dong, G.; Wang, D.; Wang, L.; Kanatzidis, M. G. $Cs_2PbI_2Cl_2$, all-inorganic two-dimensional Ruddlesden–Popper mixed halide perovskite with optoelectronic response. *J. Am. Chem. Soc.* **2018**, *140*, 11085–11090.